Lab on a Chip

RSC Publishing

PAPER

Flow switching in microfluidic networks using passive features and frequency tuning†

Cite this: *Lab Chip*, 2013, **13**, 3668

Rachel R. Collino,[a] Neil Reilly-Shapiro,[a] Bryant Foresman,[b] Kerui Xu,[c] Marcel Utz,[d] James P. Landers[ce] and Matthew R. Begley*[ab]

Received 17th April 2013,
Accepted 25th June 2013

DOI: 10.1039/c3lc50481f

www.rsc.org/loc

Manipulating fluids in microchips remains a persistent challenge in the development of inexpensive and portable point-of-care diagnostic tools. Flow in microfluidic chips can be controlled *via* frequency tuning, wherein the excitation frequency of a pressure source is matched with the characteristic frequencies of network branches. The characteristic frequencies of each branch arise from coupling between fluid in the channels and passive deformable features, and can be programmed by adjusting the dimensions and stiffness of the features. In contrast to quasi-static 'on–off' valves, such networks require only a single active element and relatively small dynamic displacements. To achieve effective flow switching between different pathways in the chip, well-separated peak frequencies and narrow bandwidths are required (such that branches are independently addressable). This paper illustrates that high selectivity can be achieved in fluidic networks that exploit fluidic inertia, with flow driven selectively at peak frequencies between ~1–100 Hz with bandwidths less than ~25% of the peak frequency. Precise frequency-based flow switching between two on-chip microchannels is demonstrated. A simple theoretical framework is presented that predicts the characteristic frequencies in terms of feature properties, thus facilitating the design of networks with specific activation frequencies. The approach provides a clear pathway to simplification and miniaturization of flow-control hardware for microchips with several fluidic domains.

Introduction

A persistent struggle in the design of bioanalytical microchips is controlling fluid flow, particularly with regard to developing methods that match the simplicity of the chips' chemical functionality. Many fully integrated bioanalytical microchips (notably those emerging for genomics) require only several fluidic domains and manipulation steps.[1,2]‡ After a sample is loaded, a typical flow sequence is to first mix the sample with isolation reagents in one domain, then transfer the fluid with simultaneous metering with additional reagents to a reaction chamber, followed by injection of a reference standard, and finally transfer to a detection domain (*e.g.*,[1]). Even for this very simple flow sequence, the control hardware associated with quasi-static 'on/off' valves can be substantial.

An attractive alternative to directly-actuated valves is to use microfluidic networks that control fluid flow *via* frequency-tuning between a periodic excitation source and the characteristic frequencies of the network's branches, significantly reducing system complexity. These frequencies are dictated by the properties of deformable features, which introduce passive solid–fluid coupling that dramatically alters network response.

Here, we describe experiments and theory motivated by the flow control concept shown in Fig. 1A, wherein a fluidic control layer is used to direct flow within a separate fluidic network embedded in a microchip. In this concept, a microchip is pressed into contact with a reconfigurable control system, with pressure pulses transmitted from the control layer to the chip through deformable films. While analogous to commonly used pneumatic valve layers, the concept here is to use entirely *passive* elements in both the chip and the control layer in conjunction with a *single* active element. Differential flow between branches in the chip is achieved by tuning the actuation frequency to match the characteristic frequencies of fluidic branches in the control layer. Hence, the control layer acts as a mechanical filter that delivers pressure to different points on the chip when different branches are activated *via* frequency tuning. This eliminates the need for

[a]*Department of Mechanical Engineering, University of California Santa Barbara, Santa Barbara, CA, 93106, USA. E-mail: begley@engr.ucsb.edu; Fax: +1 805 893 8651; Tel: +1 805 679 1122*
[b]*Materials Department, University of California Santa Barbara, Santa Barbara, CA, 93106, USA*
[c]*Department of Chemistry, University of Virginia, Charlottesville, VA, 22902, USA*
[d]*School of Chemistry, University of Southampton, Southampton SO17 1BJ, UK*
[e]*Department of Mechanical and Aerospace Engineering, University of Virginia, Charlottesville, VA, 22902, USA*

† Electronic supplementary information (ESI) available: Actuator frequency response. See DOI: 10.1039/c3lc50481f

‡ The operational requirements of such applications are much simpler than massively parallel microfluidic applications[3,4] or chips designed for combinatorial chemistries.[5]

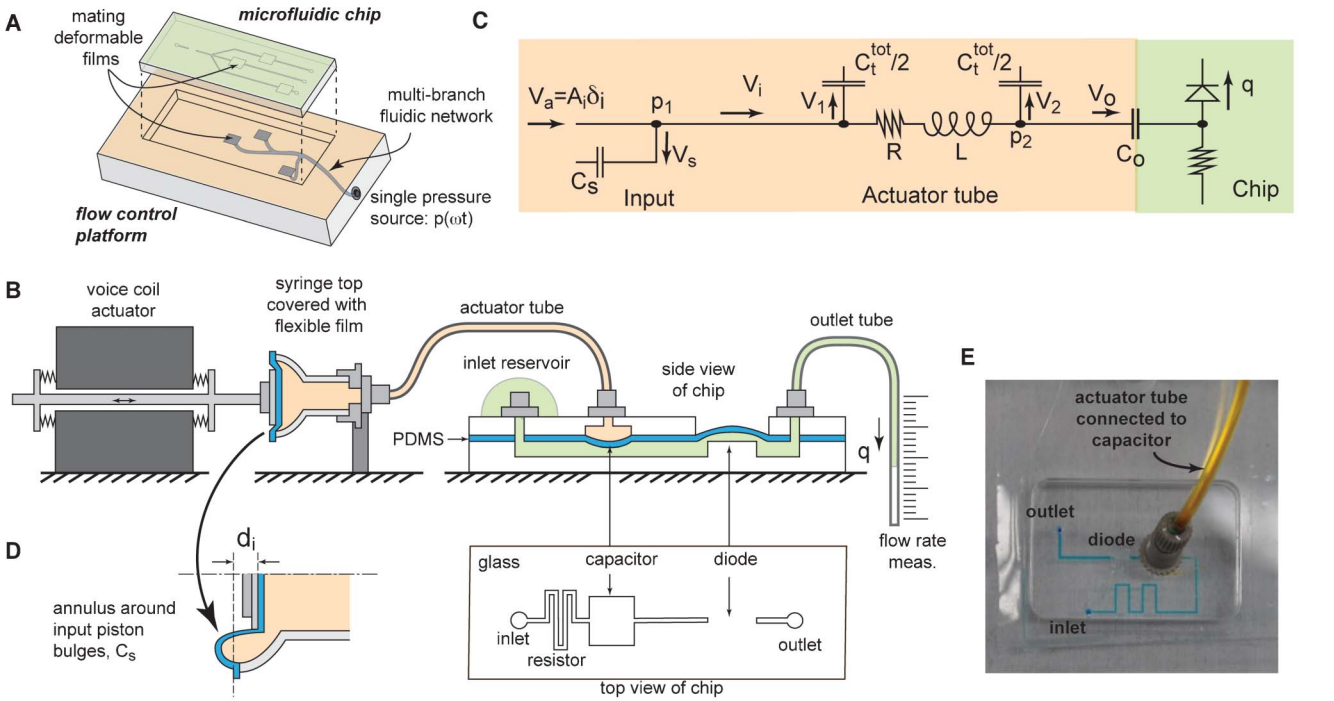

Fig. 1 Frequency-specific flow control concept and network model. (A) Schematic illustration of the flow control concept motivating the present study. The flow control platform consists of a multiply-branched fluidic network connected to a single pressure source with frequency control. The control network has multiple output nodes, which consist of small patches of deformable films: these are mated with deformable films in a disposable chip. Transfer of activation pressure to output nodes is controlled by tuning the excitation frequency to the characteristic frequency of each branch. (B) Schematic illustration of the experiment: an electromagnetic voice-coil actuator is used to apply harmonic force to a flexible film glued to a syringe cap. An actuator tube connects the syringe cap to the deformable capacitor film on the chip. The output flow rate in the chip network is measured optically. (C) The network model used to predict peak flow frequencies. To account for the fact that the tube does not experience uniform expansion due to the pressure drop in the tube, the tube capacitance (for uniform pressure) is divided between two features at the entrance and exit of the tube. (D) The flexible film connecting the voice-coil to the actuator network exhibits 'stray' capacitance due to bulging of the annulus surrounding the input piston. The chip consists of two etched networks separated by a weir that forms a diode when capped with a deformable layer. (E) Image of a circuit connected to an actuator tube.

active valves and the switching solenoids required to activate different pathways in traditional flow control schemes.

While this concept has been illustrated in previous work, the frequency response was limited to that of high-pass filters operating at low frequencies, leading to poor flow separation between channels.[6,7] Theory suggests that far more precise frequency-based flow switching can be achieved by exploiting fluidic inertia, which enables true band-pass behavior in which pressures are delivered only in a narrow range of frequencies.[7,8] Here, we validate this notion by demonstrating band-pass filters with narrow bandwidths for precise flow switching between two channels. A schematic of the device configuration is shown in Fig. 1B. An electromagnetic voice-coil is used to apply harmonic pressures at various frequencies to one end of a tube; the other end of the tube is connected to a deformable capacitor that couples this input to the chip network. In essence, the length of the tube controls the amount of fluid inertia that governs the system's frequency response. The oscillatory pressure input is converted to steady-flow components within the chip network *via* a deformable diode feature embedded in the chip's network. Critically, we show here that these passive diodes are operational over the frequency range of interest, and do not appreciably change the characteristic frequencies of the coupled networks.

The present work advances previous demonstrations of analog flow control[9–11] and micro pump designs[12,13] in several important respects: (i) the actuator is connected to the flow being driven only through passive features, greatly simplifying system fabrication/assembly, (ii) significantly better frequency-specificity is achieved here,[6,14–23] and (iii) a greater range of frequencies for a single device is illustrated, with a complementary model enabling the design of networks with predetermined peak frequencies.

Experimental methods

Device fabrication

The microfluidic devices used in this work consist of a 1.1 mm-thick Borofloat (Schott) glass "channel" layer (with the circuit features shown in Fig. 1B) and glass "actuation" layer sandwiching a poly(dimethylsiloxane) (PDMS) interlayer. Features in the glass layers were defined *via* conventional lithographic techniques and wet etching, and devices were

assembled using procedures described in ref. 1 and 6. The PDMS interlayer consisted of either a pre-cured 254 μm film (Bisco Silicones HT-6240) or a pre-cured film with an additional 160 μm spin coated and cured layer. Spin coated PDMS layers were prepared from a commercial precursor kit (Dow Corning Sylgard 184) mixed with a 10 : 1 base to curing agent ratio. A PDMS film thickness of 160 μm was achieved with two sequential coats spin coated at 750 r.p.m. on a Si substrate. Immediately prior to spin coating, a few drops of a release agent (Jersey-Cote, LabScientific, Inc.) were applied to the Si substrate and spun at 3500 r.p.m. for 30 s. After spincoating, the PDMS films were cured for 1 h at 80 °C. Film thicknesses were measured by optical interferometry (Wyko NT1100, Veeco Instruments, Inc.).

The devices were bonded as follows: the surfaces of the PDMS and glass channel layers were plasma-treated using a hand-held corona treater (Electro-Technic Products BD20-AC) for ~10 s, immediately pressed together, and baked in a 80 °C oven for several hours. Prior to bonding, the glass layers were rinsed in acetone, isopropyl alcohol, methanol, and deionized water. Diodes were defined by patterning photoresist (AZ 4210) in the weir region between the circuit channels and outlet channels; the photoresist was subsequently dissolved with acetone, leaving an unbonded strip along the weir.

Device actuation and flow rate measurements

A linear voice-coil actuator (H2W Technologies NCM02-005-4JBA, with Al housing) was used to drive the input fluidic circuit that interfaces with the microfluidic device, shown schematically in Fig. 1B. A piston attached to the voice-coil actuator drives a 254-μm-thick PDMS film that caps a syringe tip connected to a length of tubing leading to the capacitor input. The voice-coil actuator was driven by a linear amplifier assembly (H2W Technologies LCAM7-9) using a sinusoidal voltage signal generated by LabVIEW code, *via* an analog output on a USB data acquisition device (USB-6351, National Instruments). For single-tube measurements, the inlet tubing (Tygon S-54-HL, with inner/outer diameters of 1.27/2.29, 0.76/2.29, or 0.51/1.52 mm) was cut to lengths of 50, 80, 150, or 400 mm and connected to the capacitor inlet of the circuit using a Nanoport (IDEX Health & Science N-333). For branched-tube measurements, a "Y" shaped barb connector was used to create branches of 400 and 50 mm lengths connected to a circuit with two identical channels with dimensions listed in Fig. 2D. During device operation, the motion of the voice-coil actuator was monitored with a high-speed CCD laser displacement sensor (Keyence LK-G32). The dominant frequency and amplitude of the deflection signal was determined with LabVIEW code using a fast-Fourier-transform (FFT) algorithm.

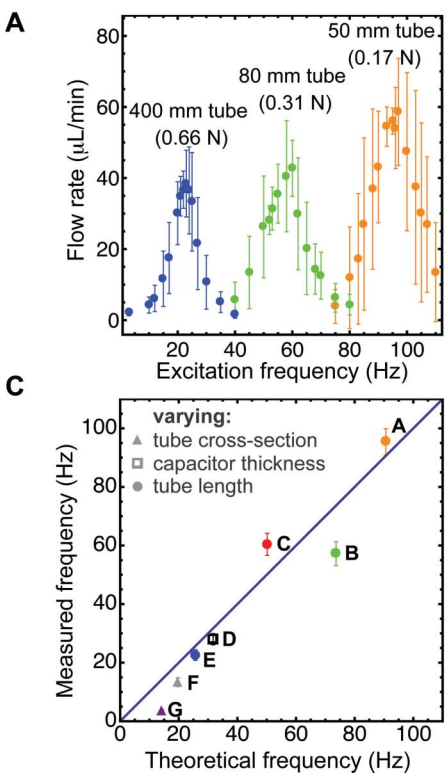

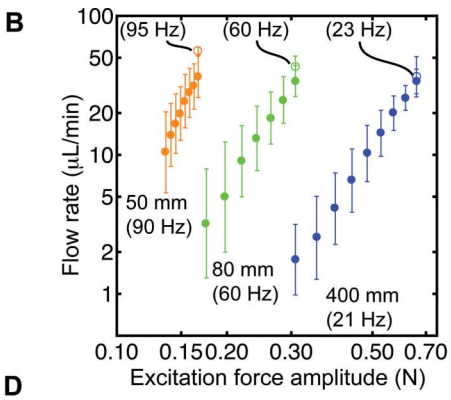

D

Point	Tube length (mm)	Tube inner/outer diameter (mm)	On-chip capacitor thickness (μm)
A	50	1.27/2.29	254
B	80	1.27/2.29	254
C	150	1.27/2.29	254
D	400	1.27/2.29	414
E	400	1.27/2.29	254
F	400	0.76/2.29	254
G	400	0.51/1.52	254

In all cases, the tube elastic modulus is 16.3±0.4 MPa, the on-chip channel depth is 100 μm, and the resistor length is 46 mm.

Fig. 2 Flow characteristics of frequency-specific circuits and comparison with the linear network model. (A) Frequency-separated flow produced with varying actuator tube lengths. The amplitude of the force supplied by the voice-coil actuator is listed in parentheses for each case. (B) Average flow rate *versus* excitation force amplitude at near-resonant driving frequencies for each input tube. For comparison, flow rate measurements at resonance are plotted as hollow circles. (C) Comparison of measured frequencies at which peak flow rate occurs *versus* those predicted by the linear model using nominal system properties and dimensions. Experimental peak frequencies between ~3 and ~100 Hz were achieved by varying the geometry of the input tubes as well as capacitor thickness on-chip. (D) Actuator tube and device properties. In all cases, error bars represent standard deviation from five measurements.

Both the microfluidic device and the actuator network were filled with a dye solution consisting of Erioglaucine disodium (acid blue 9) in water. Flow rate measurements were performed by connecting an output tube to the circuit outlet, as shown schematically in Fig. 1B. A custom LabVIEW application was used to actuate the voice-coil at frequencies ranging from ~1–180 Hz. The displacement of the fluid front was monitored with a CCD camera; image analysis was performed with ImageJ software.[24] The average flow rate at each frequency was calculated from the displacement of the fluid front using the actuation time and cross-sectional area of the outlet tube. For flow composition measurements in two-branch circuits, one circuit channel was filled with a solution of Tartrazine (acid yellow 23) in buffer (Fisher TE 10x) and the second channel filled with plain buffer solution. The solutions were collected at the circuit outlet after each run and diluted to a known volume; the flow composition was computed from absorbance measurements using a colorimeter (Vernier COL-BTA) according to the procedures described in ref. 25.

Theoretical framework

In order to elucidate the coupling between the actuation network and the chip network shown in Fig. 1B, a simple model is presented for the experimental actuator/chip assembly shown in Fig. 1C. The purpose of the model is to predict the frequencies at which flow occurs in the chip as function of the feature properties (*i.e.*, the dimensions and material stiffnesses of deformable features). For simplicity, the focus of the model is on the coupling between the activation network and the interface with the chip, and ignores additional features in the chip's network. These features do not impact the characteristic frequencies at which flow occurs; their role is explored in the discussion section. The framework combines two separate analyses: a network model (analogous to circuit analysis in electronic systems) and mechanics modeling of the deformable features, which yield the properties used in the network model.

Network model

The relationship between the characteristic frequencies of the system and the physical properties of the system can be predicted using a simple linear circuit model of the coupled tube-chip network, shown in Fig. 1C. The deformable features of the network (including the tube and deformable film at the chip/tube interface) introduce fluidic capacitance by storing and releasing fluid in response to pressure changes. The fluid used in both networks is assumed to be incompressible, such that no additional capacitance is introduced due to fluid compressibility. The actuator tube also introduces fluidic resistance (due to viscous loss) and fluidic inductance (due to inertial forces associated with accelerating flow). Strictly speaking, the diode in the chip network introduces a non-linear pressure-flow relationship (due to solid-fluid coupling[26]); here, we neglect this effect and show that characteristic frequencies are dominated by the linear response of the actuator tube and deformable film at the interface between the tube and the chip.

Derivation of the governing equations relating voice coil motion and the deflection of the on-chip capacitor (film) involves the usual application of force balance (including pressure drops associated with viscous loss and acceleration) and mass conservation.[6,7,11,19,27,28] These expressions (given as eqn (S1)–(S5) in the ESI†) can be cast in terms of two coupled second order differential equations that describe the motion of the actuator, $\delta_a(t)$, and the center-point displacement of the film connecting the actuator tube to the chip (*i.e.*, the chip capacitor), $\delta_o(t)$. This is done by defining the volume of fluid injected by the actuator motion as $V_a = A_i\delta_a$ (where A_i is the area of the input piston), and by defining the volume of fluid in the chip capacitor as $V_o = \alpha A_o\delta_o$, where A_o is the area of the chip capacitor and α is a dimensionless constant arising from analysis of the shape of the deformed chip capacitor (see next section). Using these substitutions, the governing equations for the system are given by:

$$\begin{bmatrix} m_v & 0 \\ 0 & m_f \end{bmatrix}\begin{pmatrix} \ddot{\delta}_a \\ \ddot{\delta}_o \end{pmatrix} + \begin{bmatrix} c_v & 0 \\ 0 & c_t \end{bmatrix}\begin{pmatrix} \dot{\delta}_a \\ \dot{\delta}_o \end{pmatrix} + \begin{bmatrix} k_v + k_c & -k_{12} \\ -k_{21} & k_o \end{bmatrix}\begin{pmatrix} \delta_a \\ \delta_o \end{pmatrix} = \begin{bmatrix} F_i(\omega t) \\ 0 \end{bmatrix} \quad (1)$$

where m_v and c_v are the effective mass and effective damping constant for the voice coil (due to eddy currents and friction), respectively, and $F_i(\omega t)$ is the electromagnetic force applied to the voice coil shaft. The effective mass and effective damping constant of the fluid in the tube are given by $m_f = \alpha L A_o^2$ and $c_t = \alpha R A_o^2$. The effective stiffness values are given by:

$$k_c = \frac{A_i^2}{C_s + C_t};\ k_{12} = \alpha\left(\frac{C_t + C_o}{C_o}\right)\frac{A_i A_o}{C_t + C_s} \quad (2)$$

$$k_{21} = \left(\frac{C_o}{C_o + C_t}\right)\frac{A_i A_o}{C_s + C_t};\ k_o = \alpha A_o^2\left(\frac{1}{C_t + C_o} + \frac{1}{C_s + C_t}\right) \quad (3)$$

The stiffness k_{12} reflects stray capacitance introduced by the input membrane (see next section). C_t, C_o, and C_s are the capacitance of the tube, output capacitor, and annulus, respectively. These expressions can be easily solved to yield two characteristic frequencies of the system; one is dominated by the mass and stiffness of the actuator, while the other is dominated by the effective fluid mass and stiffness of the tube and film at the tube/chip interface.

Feature properties

Here, the capacitance of the film at the tube/chip interface is estimated using the analytical result for a pressurized circular plate, which is given by:

$$C_o = \frac{3(1 - v^2)\pi a^6}{64 E h^3} \quad (4)$$

where a is the effective radius of the deformable film, E is the elastic modulus, v is the Poisson's ratio, and h is the film

thickness. The relationship between deformed volume and center-point deflection for a circular plate is $V_o = \pi a^2 \delta_o/3$, or $V_o = A_o \delta_o/3$; hence, $\alpha = 1/3$.

For the tube, the capacitance can be estimated using the mechanics solution for a pressurized tube (subject to the constraint of zero axial expansion, *i.e.*, plane strain). The total capacitance of the tube is:

$$C_t^{tot} = \frac{2\pi \ell_t R_i^2 (1+v)(R_i^2(2v-1) - R_o^2)}{E_t (R_i^2 - R_o^2)} \quad (5)$$

where ℓ_t is the length of the tube, E_t is the elastic modulus of the tube, and R_i and R_o are the inner and outer radius of the tube, respectively. In the above derivation, C_t is defined as one-half this value, *i.e.*, the capacitance due to the tube is split into equal capacitors near the entrance and outlet. The fluidic resistance and inductance of the tube, assuming fully developed steady flow, are given by:

$$R = \frac{8\mu \ell_t}{\pi R_i^4}; \; L = \frac{\rho \ell_t}{\pi R_i^2} \quad (6)$$

The capacitance of the annulus surrounding the input piston (*i.e.*, the bulging region of the syringe film) can be estimated from plate mechanics, assuming a uniform pressure acting over this region (see Fig. 1D). We have found that a 'pinned' boundary condition (which allows for the film to rotate freely along the rims where it is bonded to piston and the syringe cap) provides the best estimate for capacitance. (Assuming a clamped condition, where the film experiences zero rotation, underestimates the capacitance: the rim of the syringe cap is rather narrow and does not provide much constraint against rotation: at the rim of the piston, large deformations around the corner likely alleviate the constraint considerably.) The full plate mechanics solution for an annulus between the edges of the syringe cap and actuator piston (defined by the inner and outer radii R_i^a and R_o^a, respectively) is trivial to derive yet rather unwieldy. A more convenient expression for narrow annuli can be found by taking the limit when $\Delta R_i^a = R_o^a - R_i^a$ is small. This yields:

$$C_s = \frac{(1-v^2) R_i^a (\Delta R_i^a)^5}{Eh^3} \times \left(\frac{2}{5} + \frac{\pi}{10} \frac{\Delta R_i^a}{R_i^a} + O\left[\left(\frac{\Delta R_i^a}{R_i^a} \right)^2 \right] \right) \quad (7)$$

This result is within 1% of the exact solution for the annulus in the experiments described here.

Results

Characteristic frequencies

The frequency response for the system shown in Fig. 1B is summarized in Fig. 2 for various types of actuator tubes. Fig. 2A illustrates that output flow rate (rectified flow through the diode on-chip) exhibits band-pass behavior, selectively delivering flow at characteristic frequencies. The peak flow rate is a function of the voice-coil (input) force amplitude, as shown in Fig. 2B. Fig. 2C and 2D summarize the frequencies corresponding to peak flow rates for tubes of various types, as well as a comparison with the theoretical model.

Table 1 System response: frequency at which peak flow rate occurs (ω_f), flow rate bandwidth ($\Delta\omega_f$), frequency at which peak actuator displacement occurs (ω_a), and theoretical peak frequency for actuator displacement (ω_a^{th}). Representative data are presented in Supplementary Fig. 1 in the ESI

Point (Fig. 2C)	ω_f (Hz)	$\Delta\omega_f$ (Hz)	ω_a (Hz)	ω_a^{th} (Hz)
A	95 ± 5	20	95 ± 3	114
B	57 ± 4	17	103 ± 3	104
C	60 ± 4	26	118 ± 34	101
D	28 ± 2	10	124 ± 11	98
E	23 ± 2	13	110 ± 14	98
F	13 ± 2	10	143 ± 6	100
G	3.5 ± 0.5	4	n/a[a]	100

[a] Response over-damped.

The frequency response can be broadly modulated (with peaks ranging from ~3 and 95 Hz for this system) by varying the actuator tube length or cross-sectional area as shown in Fig. 2C. Points A, B, C, and E correspond to tubes with the same cross-sectional areas and different lengths, while points F and G correspond to tubes with the same length as E but different cross-sectional areas. Increasing the stiffness of the on-chip capacitor also produces an upward shift in peak frequency: for example, compare point D with point E: both cases have 400 mm long tubes but different capacitor film thicknesses of 414 μm and 254 μm.

This system produces two characteristic frequencies associated with the voice coil and chip capacitor; these results are presented in Table 1, with the frequency associated with the chip capacitor plotted against peak flow frequencies in Fig. 2C. Flow clearly occurs when the system is tuned to this frequency: note that flow rates are negligible when the system is tuned to the natural frequency associated with the actuator (with the exception of the case where both frequencies are comparable).

Agreement is excellent considering the simplicity of the model and the fact that there are no fitting constants in the models: nominal properties are used for all variables in the mechanics solutions. The single exception to the use of nominal values is that resistance in the tube is neglected for the predictions in Table 1 and Fig. 2C. This is justified for the present tubes which have negligible flow resistance, assuming steady flow profiles (as described in the theory section). It is well appreciated that pulsatile flow leads to velocity profiles that are quite different than those underlying the above estimates, and lead to frequency-dependent resistance that can be much larger.[29] This was explored for the present system but produced over-damped responses that are clearly not observed in experiments: we postulate that entrance effects and tube expansion alter the flow profile and eliminate the Womersley effect.[30] Finally, it should be noted that the predictions for the other natural frequency (associated with the actuator) show greater, though still reasonable, discrepan-

cies. This is likely due to imperfect alignment of the actuator assembly, which alters its stiffness.

Flow rate *vs.* forcing amplitude

To quantify flow behavior as a function of input pressure (Fig. 2B), the circuit was driven at frequencies near resonance for the 50, 80, and 400 mm input tubes. (For clarity, the maximum average flow rate, corresponding to the resonant frequency, is plotted as well). The power-law dependence of flow rate on input force amplitude is in agreement with steady-flow predictions for diodes in ref. 26 that are based on coupling between pressure magnitude, diode deformation and flow. This suggests that the solid-fluidic coupling in these diodes is not strongly influenced by dynamic flow behaviors, at least at the range of frequencies considered here. The experimental scatter is likely due to variations in actuator alignment and the background pressures introduced to the network during assembly.

It is interesting to note that the motion of the film at the tube/chip interface is quite small. Though not directly quantified in the present experiments, one can obtain an upper bound for the motion of this film by equating the volume delivered per cycle in the chip network to the volume associated with the film motion. This leads to estimates of film motion on the order of several microns, which is much smaller than the motion of the voice coil; this is a consequence of the stray capacitance in the system (*i.e.*, that of the tube itself and annulus around the input piston), which absorbs much of the injected volume and prevents its delivery to the tube/chip interface. One infers the motion of the diode film in the chip network is even smaller. This strongly points to viscous losses in the diode as the mechanism controlling bandwidth.

Flow switching

To demonstrate that flow switching can be achieved for a two-channel microchip using a single actuator and frequency tuning, a branched input tube was used to simultaneously deliver a periodic pressure input to two deformable features connected to two separate but identical branches in the chip (as shown in Fig. 3A and 3B). The average flow rate and flow composition *versus* excitation frequency is shown in Fig. 3C and 3D, illustrating precise flow switching behavior between each branch, with only a narrow frequency range (~30–40 Hz) in which flow output is comparable. Further studies are underway to investigate the full potential of metering and mixing using different combinations of input tube branches and complex excitation signals. For example, it is reasonable to expect that highly effective metering can be achieved by exciting both networks simultaneously using a compound excitation signal involving two frequencies and two amplitudes.

Discussion

The results presented here demonstrate that frequency-based flow control in microchips with three functional domains can be immediately realized, for example using channel frequencies of ~20, ~60 and ~100 Hz created by features similar to those illustrated in Fig. 2. The observed bandwidths are sufficiently narrow to make branches with these frequencies independently addressable, as shown in Fig. 3. The flow rates illustrated in Fig. 2 and 3 are well within the range needed for bioanalytical microchips, with actuation parameters that can be obtained readily using off-the-shelf components. It should be emphasized that many diagnostic applications will not require either greater selectivity or a broader frequency range than that demonstrated here. The feasibility of using frequency tuning for flow control chips with up to 10 functional domains (operating between ~5–300 Hz, with ~25 Hz separations) is very promising, considering that additional performance gains are likely possible through feature optimization.

Naturally, the upper limit of the accessible frequency range and lower limit on bandwidth are central concerns for applications requiring complex microchips with a larger number of functional domains. The models detailed above suggest that one can easily construct branches with frequencies in the range of several hundred Hz by exploiting stiffer materials (*e.g.*, glassy polymers such as polystyrene, poly (methyl methacrylate) or polycarbonate). All things being equal, these stiffer systems would expand the frequency range and also have much smaller bandwidths. The emergence of laser manufacturing and high precision computer numerical

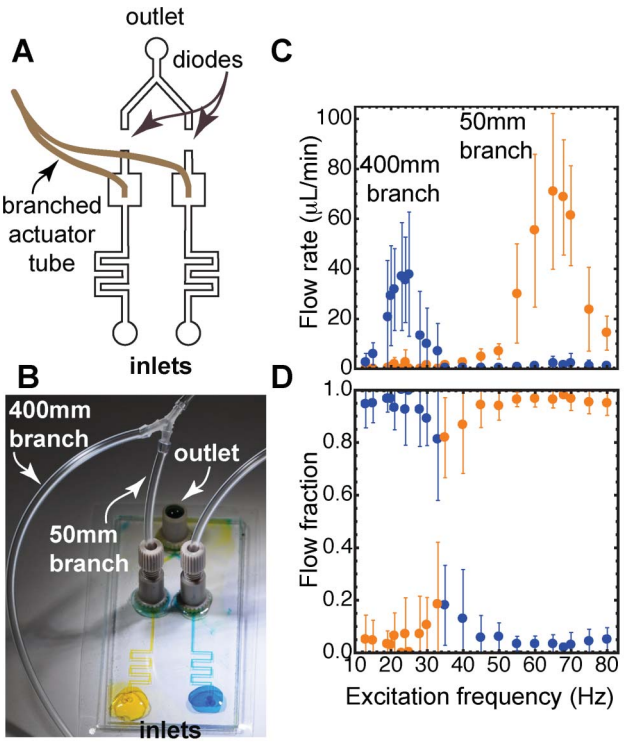

Fig. 3 Frequency-modulated flow switching in a two-branch network. (A) Schematic and (B) image of a chip with two identical circuit channels actuated with a single input tube with 50 mm and 400 mm branches. (C) Flow rate and (D) flow composition *versus* excitation frequency. Error bars represent standard deviation from four measurements.

control (CNC) milling facilitates the fabrication of compact activation platforms from such materials, with the requisite millimeter-scale channels (to replace the tubing considered here).

Future study is needed to determine if such high frequency networks can be realized; there are several issues not considered here that will likely play a role. First, one suspects that Womersley effects may be more prominent for stiff systems, leading to increased (and possibly unacceptable) damping levels. This is an open issue, since higher frequency systems can exploit shorter channels with larger cross-sectional areas, which would mitigate this effect. Second, the high frequency behavior of passive features that serve as diodes is unknown: while the present results are very promising (in that the diodes function well up to at least 100 Hz), clearly there is a limit wherein inertial effects of the diode film will attenuate the response. Further, stray capacitance of the diodes in the chip network (associated with the time to fill and empty the diodes) reduces bandwidth. This may lead to difficulties in achieving appreciable flows at higher frequencies, due to the inherent performance of the rectifiers in the chip network. Again, this is an open issue, since the required motion of the diode films in the chip network to achieve effective selectivity has not been quantified. However, the flow rates obtained for the present system suggest that the diodes will function as effective rectifiers even for very small motions.

Conclusions

We have demonstrated a highly-frequency-specific, passive flow control method using a simple tube network driven by a single voice-coil actuator. A complementary theoretical framework was presented that addresses solid-fluid coupling in dynamic flow conditions, and we show that peak frequencies may be predicted using a linear network model. This approach represents a significant step toward enabling modular control platforms, with reconfigurable input networks and frequency outputs, which could interface with multiple chip designs for portable diagnostic and forensic applications.

Acknowledgements

The authors gratefully acknowledge support from the National Institutes of Health through award R01 EB011591.

References

1 C. J. Easley, J. M. Karlinsey, J. M. Bienvenue, L. A. Legendre, M. G. Roper, S. H. Feldman, M. A. Hughes, E. L. Hewlett, T. J. Merkel, J. P. Ferrance and J. P. Landers, *Proc. Natl. Acad. Sci. U. S. A.*, 2006, **103**, 19272–19277.
2 U. Bilitewski, M. Genrich, S. Kadow and G. Mersal, *Anal. Bioanal. Chem.*, 2003, **377**, 556–569.
3 T. Thorsen, S. J. Maerkl and S. R. Quake, *Science*, 2002, **298**, 580–584.
4 R. F. Ismagilov, D. Rosmarin, P. J. A. Kenis, D. T. Chiu, W. Zhang, H. A. Stone and G. M. Whitesides, *Anal. Chem.*, 2001, **73**, 4682–4687.
5 Z. T. F. Yu, K.-i. Kamei, H. Takahashi, C. J. Shu, X. Wang, G. W. He, R. Silverman, C. G. Radu, O. N. Witte, K.-B. Lee and H.-R. Tseng, *Biomed. Microdevices*, 2009, **11**, 547–555.
6 D. C. Leslie, C. J. Easley, E. Seker, J. M. Karlinsey, M. Utz, M. R. Begley and J. P. Landers, *Nat. Phys.*, 2009, **5**, 231–235.
7 M. R. Begley, M. Utz, D. C. Leslie, H. Haj-Hariri, J. Landers and H. Bart-Smith, *Appl. Phys. Lett.*, 2009, **95**, 203501.
8 M. Utz, M. R. Begley and H. Haj-Hariri, *Lab Chip*, 2011, **11**, 3846–3854.
9 B. Mosadegh, C.-H. Kuo, Y.-C. Tung, Y.-s. Torisawa, T. Bersano-Begey, H. Tavana and S. Takayama, *Nat. Phys.*, 2010, **6**, 433–437.
10 B. Mosadegh, T. Bersano-Begey, J. Y. Park, M. A. Burns and S. Takayama, *Lab Chip*, 2011, **11**, 2813–2818.
11 K. W. Oh, K. Lee, B. Ahn and E. P. Furlani, *Lab Chip*, 2012, **12**, 515–545.
12 D. J. Laser and J. G. Santiago, *J. Micromech. Microeng.*, 2004, **14**, R35–R64.
13 S. M. Langelier, D. S. Chang, R. I. Zeitoun and M. A. Burns, *Proc. Natl. Acad. Sci. U. S. A.*, 2009, **106**, 12617–12622.
14 M. A. Unger, H.-P. Chou, T. Thorsen, A. Scherer and S. R. Quake, *Science*, 2000, **288**, 113–116.
15 T.-Q. Truong and N.-T. Nguyen, *J. Micromech. Microeng.*, 2004, **14**, 632–638.
16 J. Kim, C. Kang and Y. Kim, *Microelectron. Eng.*, 2004, **71**, 119–124.
17 C. Yamahata, C. Lotto, E. Al-Assaf and M. Gijs, *Microfluid. Nanofluid.*, 2005, **1**, 197–207.
18 J. J. Loverich, I. Kanno and H. Kotera, *Lab Chip*, 2006, **6**, 1147–1154.
19 D. Kim, N. C. Chesler and D. J. Beebe, *Lab Chip*, 2006, **6**, 639–644.
20 C.-W. Huang, S.-B. Huang and G.-B. Lee, *J. Micromech. Microeng.*, 2006, **16**, 2265–2272.
21 Y.-N. Yang, S.-K. Hsiung and G.-B. Lee, *Microfluid. Nanofluid.*, 2009, **6**, 823–833.
22 J. Ni, F. Huang, B. Wang, B. Li and Q. Lin, *J. Micromech. Microeng.*, 2010, **20**, 095033.
23 J. Ni, B. Li and J. Yang, *Microelectron. Eng.*, 2012, **99**, 28–32.
24 W. S. Rasband, *ImageJ*, U. S. National Institutes of Health, Bethesda, Maryland, USA, http://imagej.nih.gov/ij/.
25 D. C. Leslie, B. A. Melnikoff, D. J. Marchiarullo, D. R. Cash, J. P. Ferrance and J. P. Landers, *Lab Chip*, 2010, **10**, 1960–1966.
26 E. Seker, D. C. Leslie, H. Haj-Hariri, J. P. Landers, M. Utz and M. R. Begley, *Lab Chip*, 2009, **9**, 2691–2697.
27 D. J. Beebe, G. A. Mensing and G. M. Walker, *Annu. Rev. Biomed. Eng.*, 2002, **4**, 261–286.
28 R. Zengerle and M. Richter, *J. Micromech. Microeng.*, 1994, **4**, 192–204.
29 S. Vedel, L. H. Olesen and H. Bruus, *J. Micromech. Microeng.*, 2010, **20**, 035026.
30 J. Womersley, *J. Physiol. (Lond.)*, 1955, **127**, 553–563.

